ACS APPLIED POLYMER MATERIALS

pubs.acs.org/acsapm

Article

4D-Printed Resins and Nanocomposites Thermally Stimulated by Conventional Heating and IR Radiation

A. Cortés,* Jose L. Aguilar, A. Cosola, Xoan Xosé Fernández Sanchez-Romate, A. Jiménez-Suárez, M. Sangermano, M. Campo, and Silvia G. Prolongo

Cite This: *ACS Appl. Polym. Mater.* 2021, 3, 5207−5215

Read Online

ACCESS | Metrics & More | Article Recommendations | Supporting Information

ABSTRACT: The shape memory (SM) capabilities of nanocomposites based on two photocurable acrylated/methacrylated resins, doped with carbon nanotubes (CNTs), and manufactured by digital light processing 3D printing were investigated. The mechanical properties and glass transition temperature (T_g) can be tailored in a broad range by varying the weight ratio of the two resins (T_g ranging from 15 to 190 °C; Young's modulus from 1.5 to 2500 MPa). Shape fixity (S_F) and recovery (S_R) ratios are strongly influenced by the temperature being significantly higher at temperatures close to the T_g. The results confirm that the S_F strongly depends on the stiffness of chain segments between cross-linking points, whereas the S_R mainly depends on the cross-link density of the network. CNT addition barely affects the S_F and S_R in the conventional oven, whereas the recovery speed using IR heating is significantly increased for the doped nanocomposites due to their higher IR absorbance.

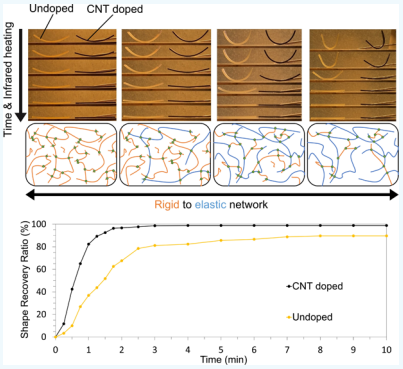

KEYWORDS: *shape memory, 4D printing, additive manufacturing, carbon nanotubes, nanocomposites*

1. INTRODUCTION

In the near future, additive manufacturing could supersede some traditional manufacturing techniques for a wide range of applications.[1] Regarding thermosetting resins, vat photopolymerization 3D printing technologies are the most developed ones.[2,3] Moreover, new photopolymerizable systems are being explored in order to improve the mechanical performance of light-cured thermosets and broaden their application fields.

In this regard, the processing of 3D-printable shape memory materials (SMMs), recently named 4D printing[4−7] (where the fourth dimension is time), is being explored. This technique allows the manufacturing of smart materials, whose programmed shape is finally deployed by an external stimulus.[8,9] Over the past 2 decades, SMMs based on metal alloys, ceramics, and polymers were developed. Particularly, shape memory polymers (SMPs) are smart polymers able to return from a deformed configuration (temporary shape) to their original state (permanent shape) when triggered by an external stimulus, such as temperature (thermo-responsive), water (pH-responsive), light (photoresponsive), and mechanical load (mechano-responsive).[10−14]

Most of the SMPs are based on thermo-responsive systems. Here, the triggering, switching, or transformation temperature (T_{trans}), which enables the recovery from the temporary to the permanent shape, is usually related to the glass transition temperature (T_g) of the thermosetting polymers. First, the polymer is deformed at $T > T_{trans}$ to program the temporary shape. In this state, the chain segments between cross-linking points adapt to the external load by conformational rearrangements, storing the strain energy when cooling down the specimen, at $T < T_{trans}$, under fixed deformation. Thus, the permanent state is restored by reheating above the T_{trans}. Some of the last research studies published about these systems[15−17] are related to different strategies to tailor the network in order to control the T_{trans}, while keeping excellent mechanical properties, such as the desired stiffness in the glassy and rubbery states. It is worth noting that the usual high stiffness of thermosets could restrict the design freedom of the temporary shape. One common strategy to reduce the rigidity is to modify the stoichiometry of reactive monomers.[18] Another interesting approach is to combine hard and soft networks, in order to control the modulus at low and high temperatures.[19] On the other hand, the conventional thermal stimulus reduces the possible future applications because of the need for using complex external heating sources.

In order to expand the future applications of 4D-printed designs, in this paper, infrared heating is exploited to trigger a shape memory (SM) cycle[20,21] comparing it to a conventional

Received: August 6, 2021
Accepted: September 17, 2021
Published: September 30, 2021

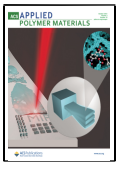

https://doi.org/10.1021/acsapm.1c00970
ACS Appl. Polym. Mater. 2021, 3, 5207−5215

heating process carried out in a conventional oven. Light is a cheap energy source, which can be remotely controlled and selectively located onto specific areas, without interfering with other parts of the structure.[22] The main advantage of using an IR lamp instead of a conventional oven lies in the possibility of performing the SM cycle *in situ* because an IR lamp is simpler and more portable equipment. In addition, it can be used for bigger structures regardless of geometry and size. Furthermore, the addition of black graphitic nanofillers should enhance the efficiency of the infrared heating due to the higher absorbance of IR radiation. As far as the authors know, the novelty of this work lies in the in-depth study of the SM properties of 3D printable mixtures based on rigid elastic networks as a function of the heating source (IR lamp and conventional oven) and curvature radius.

2. MATERIALS AND METHODS

2.1. Materials. Two different commercial resins supplied by Formlabs, both based on methacrylated oligomers and acrylated monomers, were mixed in different weight ratios. On the one side, the High Temperature Resin (HT) presents a high Young's modulus (around 3.5 GPa) and a heat deflection temperature around 298 °C under a 0.45 MPa stress. On the other hand, the Elastic Resin (ER) presents a failure strain of 160% and an ultimate tensile strength of 3.2 MPa, much lower than the 51.1 MPa of the HT resin. The different HT/ER ratios used in this study were 100:0, 80:20, 50:50, 20:80, and 100:0. NC7000 multiwall carbon nanotubes (MWCNTs) supplied by Nanocyl present a length of up to 1.5 μm, an average diameter of 9.5 nm with a 90% carbon purity, and high UV resistance. CNTs were added in an amount of 0.1 wt % because it is the limit of printability with the available equipment due the UV shielding effect.[23] In this regard, CNTs absorb part of the UV radiation, limiting the curing depth during the printing process, making it more difficult.[24]

2.2. Manufacturing of 3D-Printed Specimens. Before carrying out the 3D printing of the nanocomposite specimens, a calendering process was performed to disperse the CNTs into the different HT/ER resin mixtures. The calendering process, which was previously optimized by Jimenez-Suarez et al.,[25] consists of performing a seven-cycle process with an Exakt 80E equipment with a progressive reduction of gap distance between rollers cycle after cycle while keeping the speed of the rollers constant.

Then, the resin mixture was poured into the vat of a digital light processing (DLP) 3D printer (B9Creator by B9Creations). DLP consists of obtaining a three-dimensional object by curing, layer by layer, a photocurable formulation with UV light emitted by a digital projector. The most relevant parameters of the printing process used in the present study are a layer thickness of 30 μm, an XY plane resolution around 30 μm, and an exposure time per layer of 5.12 s, suitably set to avoid sub- or overcuring effects.[23] The projector of the 3D printer, modified D912HD equipment from Vivitek, irradiates the vat with 170 mW/cm^2 in the 380−800 nm range.[26]

Finally, two post-curing stages were carried out for the 3D-printed specimens: first, a UV post-curing stage in a B9A-LCB-020 UV oven by B9Creations at room temperature for 30 min, and then, a thermal post-curing treatment in a conventional oven at 200 °C for 1 h.

2.3. Characterization of Mixtures and Nanocomposites. *2.3.1. Photorheological Characterization.* Real-time photorheological measurements were carried out using an Anton PAAR Modular Compact Rheometer (Physica MCR 302) in a parallel-plate configuration (gap between the plates set to 0.2 mm) equipped with a UV-light source (Hamamatsu LC8 lamp, 4 mW/cm^2) underneath the bottom plate. Oscillatory tests were performed within the linear viscoelastic region of the liquid formulation setting a strain amplitude of 10% (according to the preliminary amplitude sweep experiments) and keeping the sample under a constant angular frequency (ω = 10 rad/s). All the measurements were performed at room temperature (25 °C). The photopolymerization kinetics of the precursor formulations was evaluated by recording the evolution of the viscoelastic modulus of the material as a function of the irradiation time. The induction time (the time required to induce photocross-linking) and the gel point (transition point from the liquid resin to the solid thermosetting network, taken as the intersection between the storage modulus, G', and loss modulus, G'', curves) were also calculated, this data being useful for the optimization of the printing parameters (e.g., exposure time and layer thickness).[27,28]

2.3.2. Thermomechanical Characterization. Dynamic mechanical thermal analysis (DMTA) tests were carried out in the single cantilever mode configuration at a load frequency of 1 Hz on 35.0 × 12.0 × 1.7 mm^3 specimens. Equipment used in this study is Q800 supplied by TA Instruments. The temperature range was between −80 and 300 °C at 2 °C/min speed. Here, the storage modulus, E', at 25 °C and the T_g were studied as a function of the HT/ER ratio. Moreover, the cross-link density, υ_c, was obtained by the following expression

$$\upsilon_c = \frac{E'_R}{3RT} \tag{1}$$

Here, E'_R is the storage modulus of the rubbery state at a temperature, T, being T equal to 30 K above the T_g measured as the maximum of the tan δ peak and R is the gas constant.

2.3.3. Mechanical Characterization. Tensile tests were carried out for the CNT doped and undoped 3D-printed specimens, manufactured with the different HT/ER ratios. The tests were conducted under an ASTM D638 standard in a Zwick Z100 universal test machine at 5 mm/min rate. Moreover, the fracture surfaces were analyzed in a S-3400N scanning electron microscope from Hitachi. A FEGSEM Nova NanoSEM 230 from Philips was used for characterizing the CNT distribution inside the 3D-printed specimens.

2.3.4. SM Capability Characterization. The SM capability of the 3D-printed specimens was widely studied. Here, a conventional oven, Carbolite Gero PN30, was used to heat the specimens for programming the temporary shape and recovering the initial one. Both the programming and the recovering stages were carried out at two different temperatures (T_{trans}); the T_g measured as the onset of the storage modulus drop ($T_{g,\,E'}$) and measured as the maximum of tan δ ($T_{g,\,\tan\delta}$), in order to study the effect of the temperature in the SM cycle.

To fix the temporary shape, the specimen was first placed into an oven for 30 min at T_{trans} before inserting them into an aluminum mold with the desired curvature. Then, the specimen remained inside the mold for 10 min before taking the mold out of the oven. Once the mold reached room temperature (around 25 °C), the specimen was removed from the mold, obtaining the temporary shape. Finally, the specimen was placed again into the oven for 30 min at T_{trans} for recovering the initial shape.

In this regard, several molds with different curvature angles and curvature radius were manufactured (Figure 1a) for evaluating the effect of the curvature angle on the ability of the specimens (60 × 5 × 2 mm^3) to fix the temporary shape and recover the initial one. More specifically, four of these molds (45, 90, 135, and 180°) were designed to fix the temporary shape by subjecting the whole specimen to the same curvature. Moreover, the U-shape mold, 180° (U), was used for testing the SM capability of the printed specimens at a lower curvature radius. In this regard, the specific curvature angles and radius of the molds used for fixing the temporary shape are summarized in Table 1.

The ability to fix the temporary shape (shape fixity ratio, S_F) and the ability of recovering the initial one (shape recovery ratio, S_R) are obtained from expressions 2 and 3, respectively.

$$S_F\ (\%) = \left(1 - \frac{\theta_s - \theta_F}{\theta_S}\right)\cdot 100 \tag{2}$$

$$S_R\ (\%) = \frac{\theta_F - \theta_R}{\theta_F}\cdot 100 \tag{3}$$

Here, θ_s represents the angle of the mold used for fixing the temporary shape, θ_F is the angle of the fixed shape after cooling down

https://doi.org/10.1021/acsapm.1c00970
ACS Appl. Polym. Mater. 2021, 3, 5207−5215

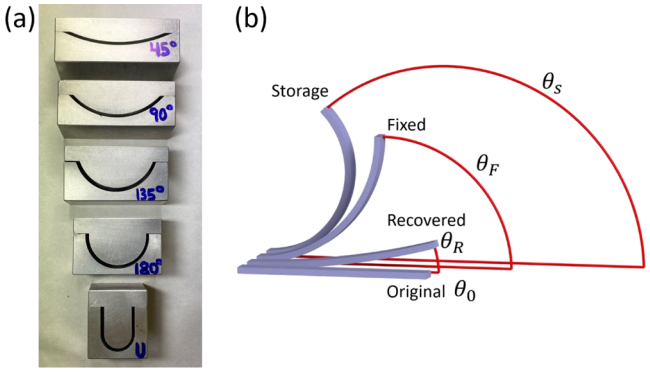

Figure 1. Molds with different curvature angles and radius for SM (a), scheme of the different stages of SM with their respective angles: the original angle of the specimen (θ_o), the storage angle (θ_s) when the specimen is inside of the mold during the heating stage; the fixed angle (θ_F) when the specimen is cooled down and removed from the mold, and the recovered angle (θ_R) obtained after the recovering stage of the initial shape (b).

Table 1. Curvature Angles and Radius of the Molds for Fixing the Temporary Shape

total angle of the mold	curvature radius, r, (mm)
45°	76
90°	38
135°	25
180°	19
180° (U)	9

the specimen, and θ_R is the angle of the recovered shape, as shown in Figure 1b. All angles were measured by image analysis with ImageJ software.

Once the optimum temperature and maximum curvature angle was studied for each HT/ER ratio by conventional heating in an oven, the SM efficiencies, S_F and S_R, for the different manufactured samples were analyzed as a function of the external heating source: conventional oven and a 1000 W IR lamp, supplied by E.VILA Projects & Supplies. The heating of an IR lamp was controlled by a temperature sensor, Sensoterm II from JP Selecta, in order to adjust the distance between the sample and lamp. The temperature control over the sample surface was ±5 °C.

3. RESULTS AND DISCUSSION

3.1. 3D Printing of Thermosetting Resins and Nanocomposites. Prior to 3D printing, the effect of CNTs onto the photopolymerization kinetics of the formulations was evaluated by means of real-time photorheology (Figure 2). All the undoped formulations, as shown in Figure 2a, showed high photoreactivity, that is, a short irradiation time required to induce cross-linking, fast curing kinetics, and a gel point achieved in few seconds (below 8 s). At a first sight, no great differences were observed among the formulations with different HT/ER ratios. However, when analyzing in detail, a slight increase in the gel time is observed when increasing the ER content (Figure 2c), which indicates a slightly lower reactivity of the ER resin with regard to the HT one. Moreover, the CNT addition to the formulations causes a delay in the onset of photocross-linking and in the achievement of the gel point, as well as slower curing kinetics, as confirmed by the lower slopes of the G' curves (Figure 2b). Here, the reduced photoreactivity of the doped formulations is due to the UV-light shielding effect of CNTs.[24] In this regard, a much higher increase in both the induction time and the gel time is observed for the doped formulations when increasing the ER content due to the hindering of the photocuring reaction because of the presence of CNTs, making more evident the less reactivity of the ER resin. Moreover, the addition of CNTs leads to an increase of the viscosity of the formulations, as confirmed by the higher G' values of the doped formulations before the onset of photocross-linking.

Furthermore, the thermomechanical properties of the 3D-printed thermosets and nanocomposites have been determined by DMTA (Figure 3). Here, the storage modulus, as shown in Figure 3a, and tan δ, as shown in Figure 3b, are shown as functions of the temperature. These results evince that the cross-linked network structure of neat photopolymerized resins are very different. It is worth noting that the thermosets obtained from the ER resin presents a sharp fall of the storage modulus and a narrow and high tan δ peak, suggesting a homogenous distribution of chain segment lengths in the network. On the other hand, the much lower and unsharpened drop of the storage modulus as a function of temperature and the broader tan δ peak of the thermosets prepared from the HT resin (from 60 °C to more than 270 °C) suggest a higher heterogeneity of the network, containing very different chain segment lengths between cross-linking points, Figure 3c shows the proposed schematic representation of the HT/ER networks.

Furthermore, the main DMTA results are shown in Figure 4. Photopolymerized thermosets from the pure HT resin presents a high E' at 25 °C, above 3.00 GPa, and a high $T_{g,\ \tan\delta}$, close to 200 °C, due to its high cross-linking degree and rigid segment chains, while thermosets prepared from the pure ER resin are much more flexible, with an E' at 25 °C of around 0.02 GPa and a low $T_{g,\ \tan\delta}$, around 15 °C. In this regard, the 3D-printed specimens show intermediate behaviors as a function of the

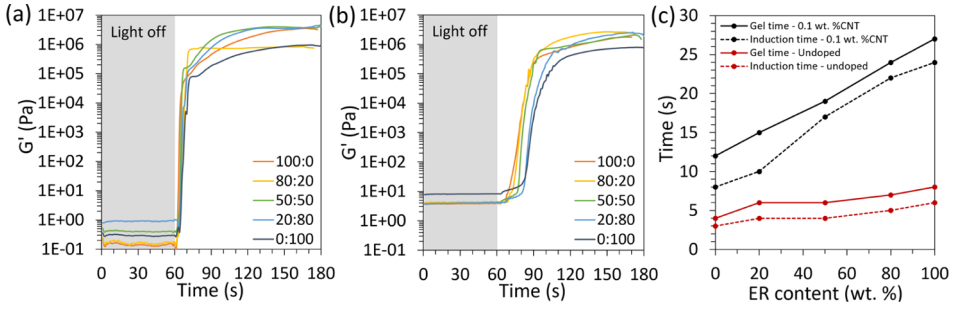

Figure 2. Photorheology tests of (a) undoped formulations, (b) 0.1 wt % CNT doped formulations, and (c) induction and gel time as a function of the HT/ER ratio.

https://doi.org/10.1021/acsapm.1c00970
ACS Appl. Polym. Mater. 2021, 3, 5207−5215

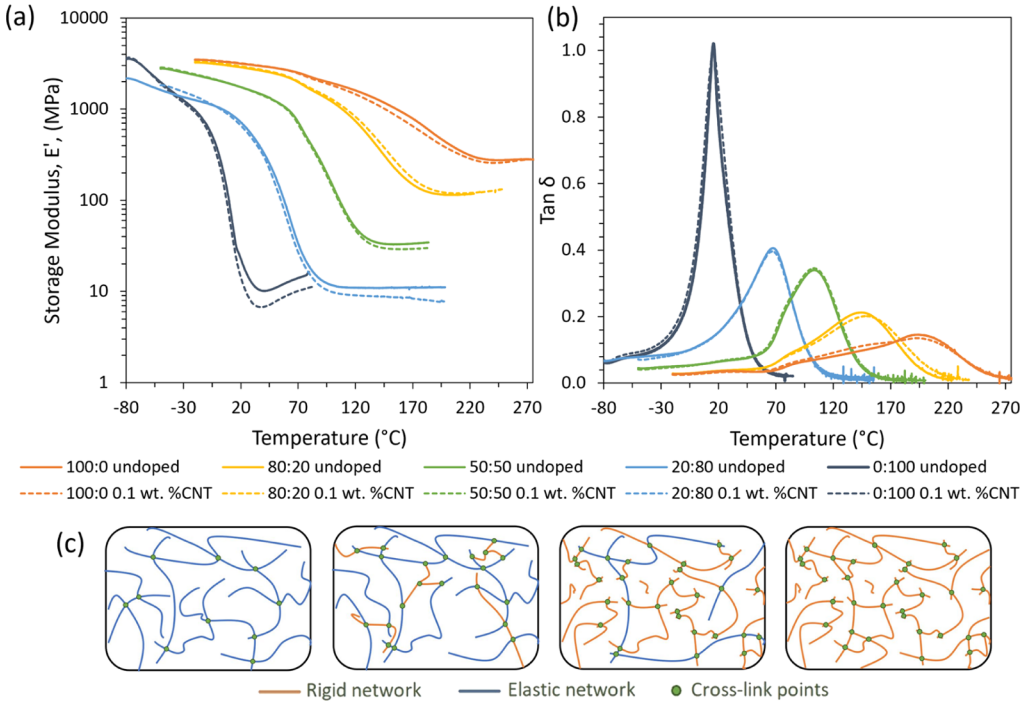

Figure 3. DMTA curves for the 4D resins and nanocomposites. Storage modulus as a function of temperature (a), tan δ as a function of temperature (b), and schemes of the different HT/ER structures (c).

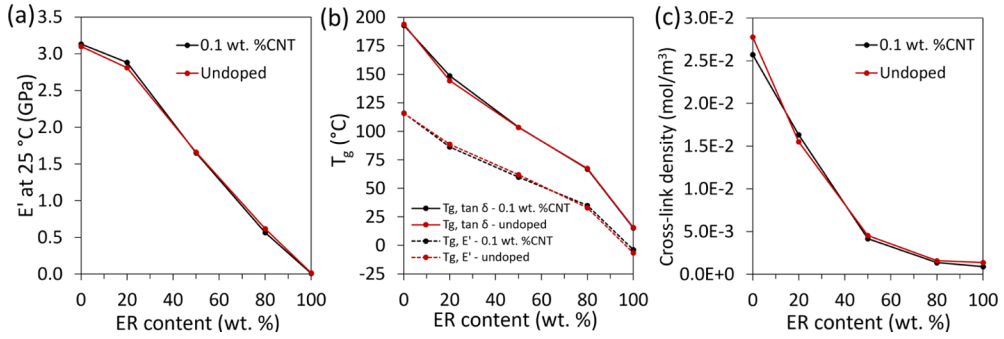

Figure 4. DMTA results: storage modulus at room temperature as a function of the HT/ER ratio (a), glass transition temperature, measured by a maximum tan δ peak and fall of storage modulus (b) and cross-link density of the network, calculated by expression 1 (c).

HT/ER ratio. The storage modulus (Figure 4a) and glass transition temperature (Figure 4b) proportionally decrease with the increase in the ER content. Here, the T_g of 3D-printed specimens was calculated both as the onset of the storage modulus drop ($T_{g,\,E'}$) and as the temperature corresponding to the maximum of the tan δ curve ($T_{g,\,\tan\delta}$). These values are closer when increasing the ER content due to the higher homogeneity of the resulting thermosetting network. Furthermore, the high difference of the cross-link density as a function of the HT/ER (Figure 4c) composition of the networks has an important influence on their SM performance, which will be addressed in further sections of this work.

In any case, DMTA results confirm that the thermomechanical properties of the 3D-printed nanocomposites are quite similar to those of the undoped specimens. No significant differences are observed from CNT addition. This means that the designed 3D printing DLP method together with the UV- and thermal postcuring treatments allow manufacturing integrated and cohesive three-dimensional structures with a similar curing degree to the undoped specimens. This conclusion is especially interesting for the printed nanocomposites doped with CNTs because they are susceptible to shielding UV radiation, leading to lower curing degrees and thus lower mechanical properties,[23,24,29] so the thermal postcuring treatment leads to an enhancement of these properties.

In addition, the mechanical behavior of the 3D-printed resins and nanocomposites was determined by tensile tests (Figure S1a), which showed even a higher stiffness (15−25% higher) and tensile strength (25−35% higher) with regard to the pristine formulations when the ER content is below or equal to 50 wt. %. More information about the mechanical properties, as the analysis of the fracture surfaces, the distribution of CNTs inside the 3D-printed specimens and the role of the UV and thermal postcuring can be found in Figures S1b,c and S2, respectively, of the Supporting Information file.

3.2. Thermally Stimulated SM by Conventional Oven.

Figures 5 and 6 show the shape fixing and recovery efficiencies, respectively. These SM tests were carried out by heating the

https://doi.org/10.1021/acsapm.1c00970
ACS Appl. Polym. Mater. 2021, 3, 5207−5215

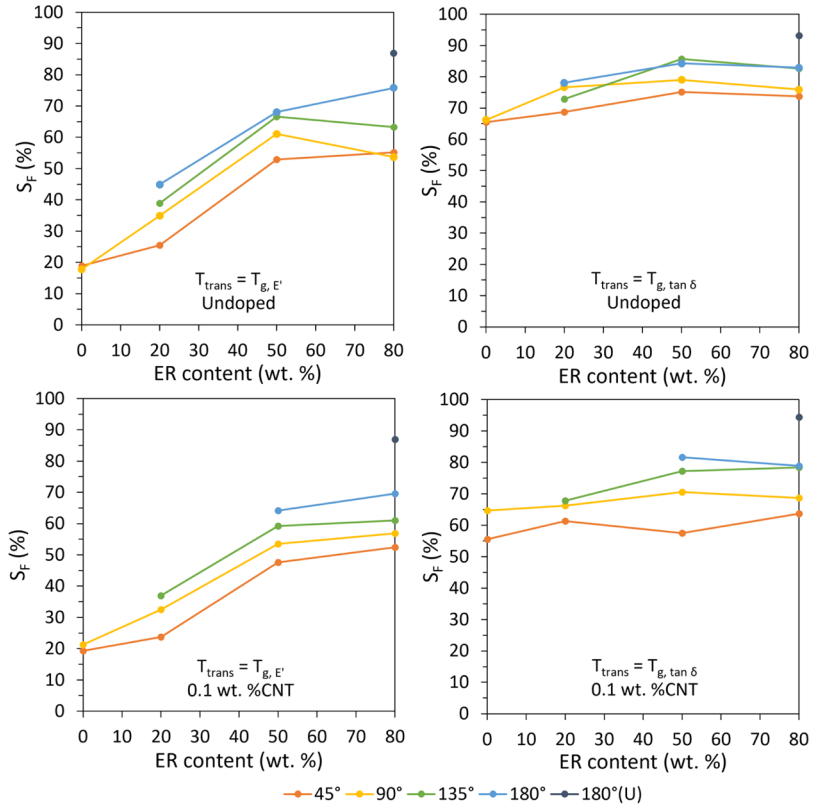

Figure 5. SM activated by conventional heating of 4D resins and nanocomposites: shape fixity ratio as a function of the resin composition, CNT addition, and the switching temperature.

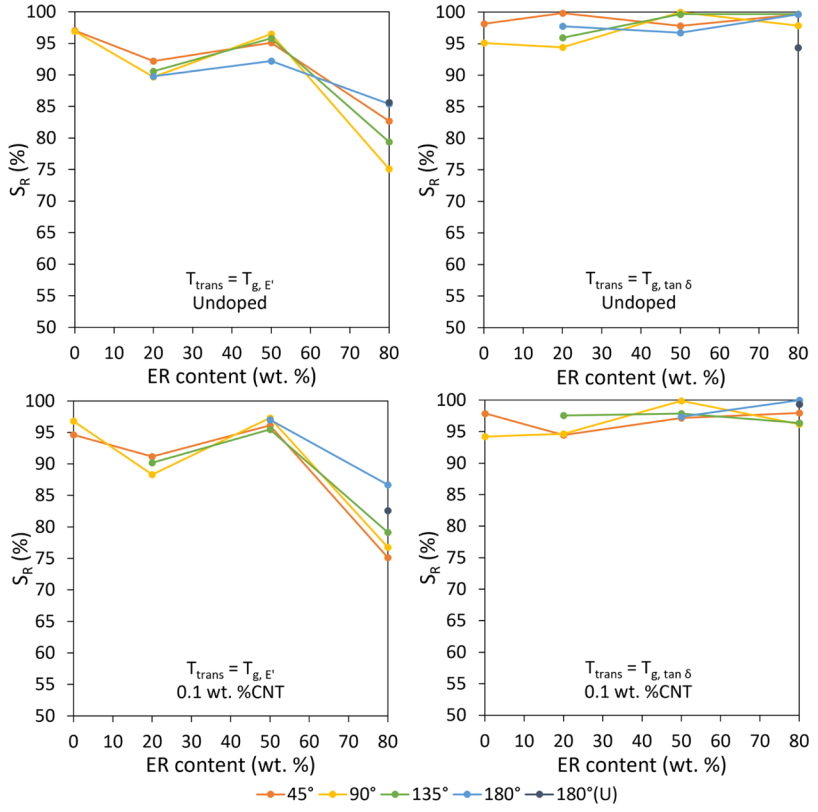

Figure 6. SM activated by conventional heating of 4D resins and nanocomposites: shape recovery ratio as a function of the resin composition, CNT addition, and the switching temperature.

https://doi.org/10.1021/acsapm.1c00970
ACS Appl. Polym. Mater. 2021, 3, 5207−5215

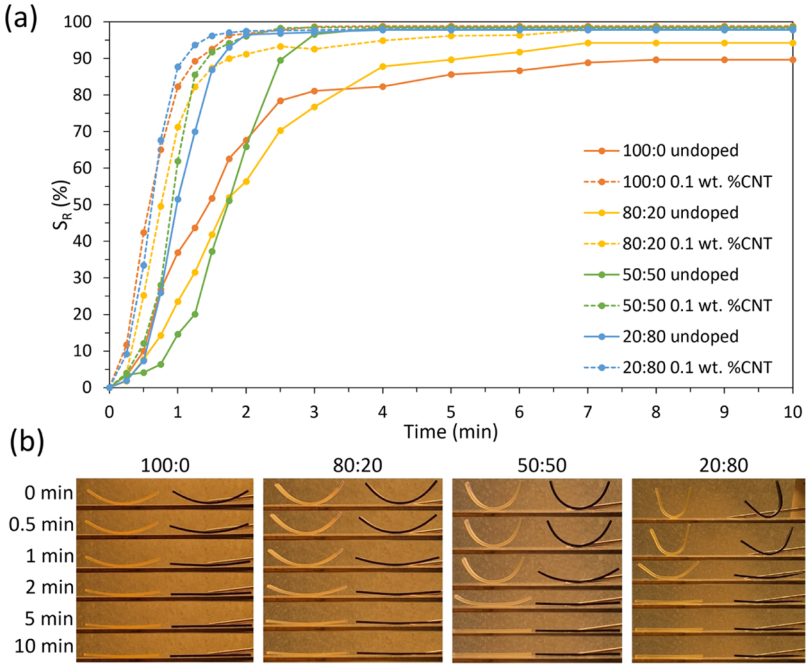

Figure 7. SM activated by IR radiation of 4D resins and nanocomposites: (a) evolution of shape recovery efficiency with irradiation time and (b) images of the shape recovery with irradiation time.

samples using a conventional oven. Here, the determination of the switching temperature for shape programming and recovery is not totally established yet. In most of the published works for this kind of systems,[11,12,30] the selected T_{trans} is usually the $T_{g,\tan\delta}$ of the SM thermosets plus a constant increment, generally T_g + 15 or 20 °C, in order to ensure the highest deformability and recovery efficiency. It is known that the network deformation reaches the maximum above the T_g, when the polymer is in its rubbery state. However, when the shape programming is done at low temperatures, the "cold-worked" specimens present improved mechanical properties.[11,31]

For these reasons, in this work, the triggering temperature (T_{trans}) has been selected as the T_g value of each HT/ER mixture, measured by DMTA as the onset of the storage modulus drop ($T_{g,E'}$) and the maximum of the tan δ peak ($T_{g,\tan\delta}$) (Figure 3b). The thermosets are reaching the rubbery state at $T_{g,\tan\delta}$, presenting a prevalent viscoelastic behavior. However, the network presents an intermediate behavior, between glassy and rubbery, at $T_{g,E'}$.

The SM behavior could not be analyzed for the thermosets prepared from the neat ER resin because of their too low T_g (below room temperature). In this regard, it is not possible to fix the temporary shape at room temperature for later recovering the original one because these polymers would be in the rubbery state during the whole SM cycle. In contrast, the most aggressive SM conditions, with high bending angles, could not be studied for the stiffer thermosets (with a high HT content) due to their brittleness. These specimens broke during bending deformation for temporary shaping. In this regard, the maximum curvatures for the 100:0, 80:20, 50:50, and 20:80 specimens were 90° (r = 38 mm), 135° (r = 25 mm), 180° (r = 19 mm), and 180° (U) (r = 9 mm), respectively. Furthermore, for the doped specimens, the maximum curvature for the 50:50 mixture is 135° instead of 180° of the undoped specimen, again related to the increased stiffness (Table S1).

As expected, the shape fixity ratio, S_F (Figure 5), increases with the switching temperature applied,[32,33] showing higher differences for the stiffer resins, with a low ER content. Moreover, S_F also increases when increasing the ER content due to the lower rubbery modulus of these thermosets[30,34] (Figure 3a). When fixing the temporary shape, the polymeric chain segments adapt to the external load by conformational rearrangements, storing the strain energy. This energy storage is more efficient with the higher elastic component of the system. The highly cross-linked network obtained from the HT resin has a strong constrained force on the polymeric chain segments, which needs more energy to fix a mechanically stable temporarily bent shape. These results are in accordance with other studies, such as Wu et al.[35]

At the highest triggering temperature, $T_{g,\tan\delta}$, the differences of S_F between 3D-printed specimens as a function of their HT/ER composition are lower, in accordance with similar studies.[35,36] The S_F also increases with the applied deformation, that is, increasing the bending angle of the mold. It is interesting to confirm that, despite higher bending deformation implying higher stored energy and therefore more stressed specimens, the shape fixing efficiency is higher.[11] The printed nanocomposites present similar SM properties to the neat thermosets due to their similar thermomechanical behavior, although their S_F tends to be slightly lower given their higher stiffness (Table S1).

On the other hand, it is interesting to point out that the S_R (Figure 6) presents a different trend. Particularly, the S_R is relatively high, above 70−80%, even at the lower triggering temperature ($T_{g,E'}$). This means that the energy required for shape recovery is lower than the one needed for programming the temporary configuration. During the fixing of the temporary shape, the chain segments between the cross-links adapt to the external load via conformational rearrangements. The stored strain energy is released when the specimen is unloaded and reheated at T_{trans}, thus restoring the permanent shape. These results are in total agreement with the study of

https://doi.org/10.1021/acsapm.1c00970
ACS Appl. Polym. Mater. 2021, 3, 5207−5215

Pandini et al.,[31] who concluded that SM recovery is governed by the cross-link density, while the stiffness of the chain segments between cross-linking points plays a minor role.[37]

In this regard, the shape recovery percentage at $T_{g,E'}$ decreases with the increase of the ER content, contrary to the trend observed for the shape fixing efficiency. As the HT content increases, the cross-link density of the thermoset network increases (Figure 3c), inducing an enhancement of the recovery efficiency.[35,37,38] This is explained by the higher stored energy during the shaping, due to the higher rearrangements of the short chain segment between cross-linking points in a HT thermoset.

The slight differences observed between the 80:20 and 50:50 HT/ER ratios at $T_{trans} = T_{g,E'}$ may be caused by the effect of T_g, which must be significantly higher than room temperature in order to guarantee a good shape fixing. In both cases, the T_g values are considerably higher than room temperature, so the results are similar despite the different HT/ER ratios. However, the 20:80 condition shows a T_g much closer to room temperature, so the shape recovery is much lower.

The shape recovery efficiency is above 94% in every case when the switching temperature is the T_g measured by the tan δ peak, in good agreement with the values already reported in the literature for other SM thermoset networks.[15,39] Moreover, no significant differences were observed between the doped and undoped specimens regarding the shape recovery efficiency triggered by conventional heating.

3.3. Infrared Radiation-Stimulated SM. SM is the smart behavior of materials with several applications, such as packaging, self-displaying, and actuators, among others.[40] However, the thermal activation of the studied polymers limits their use due to the low portability and size of conventional ovens. An infrared light lamp is an effective non-contact heating source, which allows partial or total heating, thus enabling the possibility to drive sequential or full SM processes. Therefore, both shape programming and recovery were carried out by IR radiation at $T_{g,\tan\delta}$ and the maximum curvature reached for each HT/ER ratio. In this regard, the addition of CNTs combined with the IR heating could lead to a better SM performance due to the higher IR absorbance of CNTs.

Figure 7a shows IR-triggered SM recovery as a function of irradiation time, while the recovery speed calculated from the initial linear region of the S_R curves are given in Table 2. Figure 7b shows the images of the shape recovery with irradiation time. The SM recovery driven by means of conventional heating required 15−20 min, whereas this time is reduced to 2−4 min (more than 80% reduction) when an IR lamp is used as the heating source. The conventional heating process requires more time due to the high volume of the oven, around 30 L, making the SM cycle more power-consuming for heating small specimens, while the IR lamp is directly focused on their surfaces. CNT addition significantly increases the recovery speed (94% faster than that of the undoped specimens on average) due to the higher IR absorbance of the doped specimens. The S_R values and recovery speed obtained in this study are similar to other results reported in the literature.[20,21]

Furthermore, Table 3 lists the S_F and S_R of the studied HT/ER thermosets and nanocomposites, as a function of the heating source used for performing the SM cycle. A slight decrease in the S_F is confirmed when using the IR lamp. This can be explained because the use of a conventional oven leads to volumetric heating, offering a more homogeneous heating of the specimen, while the IR lamp is focused just on the compression face of the bent specimen. Nevertheless, no great differences in the fixing and recovery efficiencies are observed as a function of the thermal source. This is expected because the stored energy mainly depends on the thermosetting network and the temporary shape and not on the thermal source or heating rate.

In any case, the S_R is higher than 94% for the nanocomposite specimens and 90% for the undoped ones. Here, the lower S_R value for the undoped specimens, 90%, was obtained when performing the SM cycle with the IR lamp, where the heating is not volumetric but just focused on the compression face of the bent specimen. Conversely, the lower S_R value for the nanocomposite specimens, 94%, was obtained when performing the SM cycle with the conventional oven, where no enhancement in heating is possible due to IR absorbance.

More specifically, IR radiation on CNT-doped specimens allows to obtain S_R ratios above 98% regardless the HT/ER ratio, demonstrating the great suitability of the studied systems for SM purposes.

Table 2. Shape Recovery Speed with the IR Lamp as a Function of the HT/ER Ratio

	shape recovery speed (% S_R/min)	
HT/ER	undoped	0.1 wt % CNT
100/0	42	94
80/20	32	78
50/50	56	98
20/80	80	105

Table 3. Comparison of Shape Fixity and Recovery Ratios Activated by Different Thermal Sources (Conventional Oven and IR Lamp) at $T_{g,\tan\delta}$ and Maximum Curvature Reached for Each HT/ER Mixture

		S_F (%)		S_R (%)	
heating source	HT/ER	undoped	0.1 wt % CNT	undoped	0.1 wt % CNT
conventional oven	100/0	66	65	95	94
	80/20	73	68	96	98
	50/50	84	82	97	97
	20/80	93	94	99	99
IR lamp	100/0	67	58	90	99
	80/20	72	68	94	98
	50/50	80	77	98	98
	20/80	84	81	98	98

4. CONCLUSIONS

Two photocurable acrylated/methacrylated resins have been used to develop 4D-printable SM materials, one (HT) resulting in thermosets with high thermal strength and stiffness and the other (ER) giving polymers with low stiffness but high elongation at break. CNTs were added to enhance both the mechanical properties and SM performance by IR heating due to their higher absorbance.

It has been observed that the thermal, mechanical, and SM behaviors can be tailored by tuning the HT/ER composition (T_g ranging from 15 to 190 °C and Young's modulus from 1.5 to 2500 MPa). In this regard, the CNT addition enhances the

https://doi.org/10.1021/acsapm.1c00970
ACS Appl. Polym. Mater. 2021, 3, 5207−5215

mechanical properties in tensile load conditions (an increment of Young's modulus of around 15−25% and an increment of tensile strength close to 25−35%) of HT/ER mixtures with an ER content equal to or less than 50%.

Thermally triggered SM measurements have been carried out by using conventional heating or IR radiation. Regarding the SM performance achieved by triggering the thermosets via conventional heating at T_{trans}, setting the temperature of the oven at $T_{g,\tan\delta}$, the high S_R (above 94%) confirmed the excellent 4D performance of the proposed systems. When setting a lower switching temperature, $T_{g,E'}$, the S_F strongly depends on the HT/ER ratio. Here, S_F increases with the ER content due to the lower rubbery modulus of these thermosets. In addition, it is also proved that the increase of the bending angle enhances the shape fixing efficiency. Oppositely, the S_R of the 3D-printed specimens decreases with the increase in the ER content due to their lower cross-linking degree.

CNT addition scarcely affects the SM process carried out in a conventional oven, whereas IR radiation significantly accelerates the shape fixing and recovery process. Moreover, this effect is even greater for nanocomposites doped with CNTs (94% faster with regard to the undoped formulations), which enhances IR absorbance, enabling the use of this easier method to carry out the SM by the final user.

■ ASSOCIATED CONTENT

Supporting Information

The Supporting Information is available free of charge at https://pubs.acs.org/doi/10.1021/acsapm.1c00970.

Tensile tests, scanning electron microscopy micrographs of fracture surfaces, and CNT distribution inside the 3D-printed specimens (PDF)

■ AUTHOR INFORMATION

Corresponding Author

A. Cortés − *Materials Science and Engineering Area, University Rey Juan Carlos, 28933 Móstoles, Madrid, Spain;* orcid.org/0000-0001-8610-3497; Phone: +34914888252; Email: alejandro.cortes@urjc.es

Authors

Jose L. Aguilar − *Materials Science and Engineering Area, University Rey Juan Carlos, 28933 Móstoles, Madrid, Spain*

A. Cosola − *Department of Applied Science and Technology, Politecnico di Torino, 10129 Turin, Italy*

Xoan Xosé Fernández Sanchez-Romate − *Materials Science and Engineering Area, University Rey Juan Carlos, 28933 Móstoles, Madrid, Spain;* orcid.org/0000-0001-9283-4712

A. Jiménez-Suárez − *Materials Science and Engineering Area, University Rey Juan Carlos, 28933 Móstoles, Madrid, Spain;* orcid.org/0000-0001-8416-6398

M. Sangermano − *Department of Applied Science and Technology, Politecnico di Torino, 10129 Turin, Italy;* orcid.org/0000-0002-8630-1802

M. Campo − *Materials Science and Engineering Area, University Rey Juan Carlos, 28933 Móstoles, Madrid, Spain*

Silvia G. Prolongo − *Materials Science and Engineering Area, University Rey Juan Carlos, 28933 Móstoles, Madrid, Spain*

Complete contact information is available at: https://pubs.acs.org/10.1021/acsapm.1c00970

Author Contributions

The manuscript was written through contributions of all authors. All authors have given approval to the final version of the manuscript.

Notes

The authors declare no competing financial interest.

■ ACKNOWLEDGMENTS

This work was supported by the Ministerio de Economía y Competitividad of Spanish Government [PID2019-106703RB-I00] and Comunidad de Madrid regional government [ADITIMAT-CM S2018/NMT-4411].

■ REFERENCES

(1) Pereira, T.; Kennedy, J. V.; Potgieter, J. A Comparison of Traditional Manufacturing vs Additive Manufacturing, the Best Method for the Job. *Procedia Manuf.* **2019**, *30*, 11−18.

(2) Bagheri, A.; Jin, J. Photopolymerization in 3D Printing. *ACS Appl. Polym. Mater.* **2019**, *1*, 593−611.

(3) Sampson, K. L.; Deore, B.; Go, A.; Nayak, M. A.; Orth, A.; Gallerneault, M.; Malenfant, P. R. L.; Paquet, C. Multimaterial Vat Polymerization Additive Manufacturing. *ACS Appl. Polym. Mater.* **2021**, *3*, 4304−4324.

(4) Ahmed, A.; Arya, S.; Gupta, V.; Furukawa, H.; Khosla, A. 4D Printing: Fundamentals, Materials, Applications and Challenges. *Polymer* **2021**, *228*, 123926.

(5) Chu, H.; Yang, W.; Sun, L.; Cai, S.; Yang, R.; Liang, W.; Yu, H.; Liu, L. 4D Printing: A Review on Recent Progresses. *Micromachines* **2020**, *11*, 796.

(6) Bagheri, A.; Ling, H.; Bainbridge, C. W. A.; Jin, J. Living Polymer Networks Based on a RAFT Cross-Linker: Toward 3D and 4D Printing Applications. *ACS Appl. Polym. Mater.* **2021**, *3*, 2921−2930.

(7) Zhang, Y.; Josien, L.; Salomon, J.-P.; Simon-Masseron, A.; Lalevée, J. Photopolymerization of Zeolite/Polymer-Based Composites: Toward 3D and 4D Printing Applications. *ACS Appl. Polym. Mater.* **2020**, *3*, 400−409.

(8) Kuang, X.; Roach, D. J.; Wu, J.; Hamel, C. M.; Ding, Z.; Wang, T.; Dunn, M. L.; Qi, H. J. Advances in 4D Printing: Materials and Applications. *Adv. Funct. Mater.* **2019**, *29*, 1805290.

(9) Nadgorny, M.; Ameli, A. Functional Polymers and Nanocomposites for 3D Printing of Smart Structures and Devices. *ACS Appl. Mater. Interfaces* **2018**, *10*, 17489−17507.

(10) Meng, H.; Li, G. A Review of Stimuli-Responsive Shape Memory Polymer Composites. *Polymer* **2013**, *54*, 2199−2221.

(11) Karger-Kocsis, J.; Kéki, S. Review of Progress in Shape Memory Epoxies and Their Composites. *Polymers* **2017**, *10*, 34.

(12) Kumar Patel, K.; Purohit, R. Future Prospects of Shape Memory Polymer Nano-Composite and Epoxy Based Shape Memory Polymer- A Review. *Mater. Today: Proc.* **2018**, *5*, 20193−20200.

(13) Momeni, F.; Hassani, S. M. M.; Liu, X.; Ni, J. A Review of 4D Printing. *Mater. Des.* **2017**, *122*, 42−79.

(14) Wong, J.; Basu, A.; Wende, M.; Boechler, N.; Nelson, A. Mechano-Activated Objects with Multidirectional Shape Morphing Programmed via 3D Printing. *ACS Appl. Polym. Mater.* **2020**, *2*, 2504−2508.

(15) Datta, S.; Henry, T. C.; Sliozberg, Y. R.; Lawrence, B. D.; Chattopadhyay, A.; Hall, A. J. Carbon Nanotube Enhanced Shape Memory Epoxy for Improved Mechanical Properties and Electroactive Shape Recovery. *Polymer* **2021**, *212*, 123158.

(16) Fan, W.; Zhang, Z.; Liu, Y.; Wang, J.; Li, Z.; Wang, M. Shape Memory Polyacrylamide/Gelatin Hydrogel with Controllable Mechanical and Drug Release Properties Potential for Wound Dressing Application. *Polymer* **2021**, *226*, 123786.

(17) Safranski, D. L.; Gall, K. Effect of Chemical Structure and Crosslinking Density on the Thermo-Mechanical Properties and Toughness of (Meth)Acrylate Shape Memory Polymer Networks. *Polymer* **2008**, *49*, 4446−4455.

(18) Belmonte, A.; Russo, C.; Ambrogi, V.; Fernández-Francos, X.; De la Flor, S. Epoxy-Based Shape-Memory Actuators Obtained via Dual-Curing of Off-Stoichiometric "Thiol-Epoxy" Mixtures. *Polymers* **2017**, *9*, 113.
(19) Ratna, D.; Karger-Kocsis, J. Recent Advances in Shape Memory Polymers and Composites: A Review. *J. Mater. Sci.* **2008**, *43*, 254−269.
(20) Leng, J.; Wu, X.; Liu, Y. Infrared Light-Active Shape Memory Polymer Filled with Nanocarbon Particles. *J. Appl. Polym. Sci.* **2009**, *114*, 2455−2460.
(21) Herath, M.; Epaarachchi, J.; Islam, M.; Fang, L.; Leng, J. Light Activated Shape Memory Polymers and Composites: A Review. *Eur. Polym. J.* **2020**, *136*, 109912.
(22) Zhang, Y.; Yin, X.-Y.; Zheng, M.; Moorlag, C.; Yang, J.; Wang, Z. L. 3D Printing of Thermoreversible Polyurethanes with Targeted Shape Memory and Precise in Situ Self-Healing Properties. *J. Mater. Chem. A* **2019**, *7*, 6972−6984.
(23) Cortés, A.; Sánchez-Romate, X. F.; Jiménez-Suárez, A.; Campo, M.; Ureña, A.; Prolongo, S. G. Mechanical and Strain-Sensing Capabilities of Carbon Nanotube Reinforced Composites by Digital Light Processing 3D Printing Technology. *Polymers* **2020**, *12*, 975.
(24) Gonzalez, G.; Chiappone, A.; Roppolo, I.; Fantino, E.; Bertana, V.; Perrucci, F.; Scaltrito, L.; Pirri, F.; Sangermano, M. Development of 3D Printable Formulations Containing CNT with Enhanced Electrical Properties. *Polymer* **2017**, *109*, 246−253.
(25) Jiménez-Suárez, A.; Campo, M.; Sánchez, M.; Romón, C.; Ureña, A. Dispersion of Carbon Nanofibres in a Low Viscosity Resin by Calendering Process to Manufacture Multiscale Composites by VARIM. *Composites, Part B* **2012**, *43*, 3104−3113.
(26) Nejadebrahim, A.; Ebrahimi, M.; Allonas, X.; Croutxé-Barghorn, C.; Ley, C.; Métral, B. A New Safranin Based Three-Component Photoinitiating System for High Resolution and Low Shrinkage Printed Parts via Digital Light Processing. *RSC Adv.* **2019**, *9*, 39709−39720.
(27) Roppolo, I.; Chiappone, A.; Angelini, A.; Stassi, S.; Frascella, F.; Pirri, C. F.; Ricciardi, C.; Descrovi, E. 3D Printable Light-Responsive Polymers. *Mater. Horiz.* **2017**, *4*, 396−401.
(28) Stassi, S.; Fantino, E.; Calmo, R.; Chiappone, A.; Gillono, M.; Scaiola, D.; Pirri, C. F.; Ricciardi, C.; Chiadò, A.; Roppolo, I. Polymeric 3D Printed Functional Microcantilevers for Biosensing Applications. *ACS Appl. Mater. Interfaces* **2017**, *9*, 19193−19201.
(29) Cortés, A.; Sánchez-Romate, X. F.; Jiménez-Suárez, A.; Campo, M.; Esmaeili, A.; Sbarufatti, C.; Ureña, A.; Prolongo, S. G. Complex Geometry Strain Sensors Based on 3D Printed Nanocomposites: Spring, Three-Column Device and Footstep-Sensing Platform. *Nanomaterials* **2021**, *11*, 1106.
(30) Liu, Y.; Han, C.; Tan, H.; Du, X. Thermal, Mechanical and Shape Memory Properties of Shape Memory Epoxy Resin. *Mater. Sci. Eng., A* **2010**, *527*, 2510−2514.
(31) Pandini, S.; Bignotti, F.; Baldi, F.; Passera, S. Network Architecture and Shape Memory Behavior of Cold-Worked Epoxies. *J. Intell. Mater. Syst. Struct.* **2013**, *24*, 1583−1597.
(32) Yu, K.; Ge, Q.; Qi, H. J. Reduced Time as a Unified Parameter Determining Fixity and Free Recovery of Shape Memory Polymers. *Nat. Commun.* **2014**, *5*, 3066.
(33) Song, J. J.; Chang, H. H.; Naguib, H. E. Biocompatible Shape Memory Polymer Actuators with High Force Capabilities. *Eur. Polym. J.* **2015**, *67*, 186−198.
(34) Lee, B. S.; Chun, B. C.; Chung, Y.-C.; Sul, K. I.; Cho, J. W. Structure and Thermomechanical Properties of Polyurethane Block Copolymers with Shape Memory Effect. *Macromolecules* **2001**, *34*, 6431−6437.
(35) Wu, X. L.; Kang, S. F.; Xu, X. J.; Xiao, F.; Ge, X. L. Effect of the Crosslinking Density and Programming Temperature on the Shape Fixity and Shape Recovery in Epoxy-Anhydride Shape-Memory Polymers. *J. Appl. Polym. Sci.* **2014**, *131*, 40559.
(36) Huang, W. M.; Zhao, Y.; Wang, C. C.; Ding, Z.; Purnawali, H.; Tang, C.; Zhang, J. L. Thermo/Chemo-Responsive Shape Memory Effect in Polymers: A Sketch of Working Mechanisms, Fundamentals and Optimization. *J. Polym. Res.* **2012**, *19*, 9952.
(37) Wei, K.; Zhu, G.; Tang, Y.; Liu, T.; Xie, J. The Effects of Crosslink Density on Thermo-Mechanical Properties of Shape-Memory Hydro-Epoxy Resin. *J. Mater. Res.* **2013**, *28*, 2903−2910.
(38) Koerner, H.; Strong, R. J.; Smith, M. L.; Wang, D. H.; Tan, L.-S.; Lee, K. M.; White, T. J.; Vaia, R. A. Polymer Design for High Temperature Shape Memory: Low Crosslink Density Polyimides. *Polymer* **2013**, *54*, 391−402.
(39) Mora, P.; Schäfer, H.; Jubsilp, C.; Rimdusit, S.; Koschek, K. Thermosetting Shape Memory Polymers and Composites Based on Polybenzoxazine Blends, Alloys and Copolymers. *Chem. - Asian J.* **2019**, *14*, 4129−4139.
(40) Bogue, R. Shape-memory materials: a review of technology and applications. *Assemb. Autom.* **2009**, *29*, 214−219.

https://doi.org/10.1021/acsapm.1c00970
ACS Appl. Polym. Mater. 2021, 3, 5207−5215